Available online at www.sciencedirect.com
SCIENCE DIRECT®
International Journal of Heat and Fluid Flow 26 (2005) 191–203
International Journal of HEAT AND FLUID FLOW
www.elsevier.com/locate/ijhff

Large-eddy simulation of turbulent flow in a concentric annulus with rotation of an inner cylinder

Seo Yoon Chung, Hyung Jin Sung *

Department of Mechanical Engineering, Korea Advanced Institute of Science and Technology, 373-1, Guseong-dong, Yuseong-gu, Daejeon 305-701, Republic of Korea

Received 18 November 2003; accepted 18 August 2004

Abstract

Large-eddy simulations of the turbulent flow in a concentric annulus with inner wall rotation were performed at $Re_{D_h} = 8900$ for three rotation rates ($N = 0.2145$, 0.429 and 0.858). The main emphasis of this work was on the destabilization of the near-wall turbulent structures due to rotation of the inner wall. The turbulent structures close to the inner wall were scrutinized by computing the lower-order statistics. The anisotropy invariant map for the Reynolds stress tensor and the invariant function revealed that rotation of the inner wall altered the anisotropy of the turbulent structure. The probability density functions of the velocity fluctuations and the splat/anti-splat process were examined to create a more complete picture of the contributions of the flow events to turbulent production. The present numerical results indicate that the alteration of the turbulent structures can be attributed to the destabilizing effect of rotation of the inner wall, which gives rise to an augmentation of sweep and ejection events.

Keywords: Large-eddy simulation; Concentric annulus; Turbulent rotating flow; Destabilizing effect

1. Introduction

Concentric annular pipe flow with rotation of the inner wall is often encountered in engineering applications such as chemical mixing devices, turbo machinery, bearings, rotating-tube heat exchangers, and the drilling of oil wells. In addition to the practical implications of achieving a better understanding of this type of flow, the study of turbulent rotating flows in concentric annuli provides insight into the general problem of three-dimensional turbulent boundary layers (TBLs).

Numerous experimental and numerical studies have examined rotating flows in concentric annuli. Taylor (1923) first investigated the stability of the flow between two concentric rotating cylinders. He found that when the inner cylinder is at rest and the outer cylinder is rotated, the flow is stable, but that when the inner cylinder is rotated and the outer cylinder is at rest, the flow is unstable. The combined axial and rotational flow in an annulus with a rotating inner wall was studied experimentally by Kaye and Elgar (1958). They identified the following basic flow regimes in the annular gap: laminar flow; laminar flow with vortices; turbulent flow; and turbulent flow with vortices. Yamada (1962) showed that the pressure loss increased sharply when the inner shaft was rotating and decreased with increasing axial bulk flow. Recently, Nouri and Whitelaw (1994) and Escudier and Gouldson (1995) measured the mean velocities and the Reynolds shear stresses of Newtonian and non-Newtonian fluids by Laser Doppler Velocimetry (LDV). Numerical simulations of turbulent flows through concentric annuli with rotating inner walls have been performed by many researchers. Sharma et al. (1976) investigated the flow field in such systems

* Corresponding author. Tel.: +82 42 869 3027; fax: +82 42 869 5027.
E-mail address: hjsung@kaist.ac.kr (H.J. Sung).

0142-727X/$ - see front matter © 2004 Elsevier Inc. All rights reserved.
doi:10.1016/j.ijheatfluidflow.2004.08.006

Nomenclature

A_b invariant function $= -(\mathrm{III}_b/2)/(\mathrm{II}_b/3)^{3/2}$
a_1 structure parameter $= (\overline{v'_r v'_z}^2 + \overline{v'_r v'_\theta}^2 + \overline{v'_\theta v'_z}^2)^{1/2}/2k$
b_{ij} Reynolds stress anisotropy tensor $= \overline{u'_i u'_j}/2k - \delta_{ij}/3$
C model coefficient
C_f skin friction coefficient $= \tau_z/(1/2)\rho V_\mathrm{m}^2$
D_h hydraulic diameter $= 4\delta$
F invariant function $= 1 + 9\mathrm{II}_b + 27\mathrm{III}_b$
G invariant function $= (1/9)F$
k turbulent kinetic energy $= 0.5(\overline{v'^2_r} + \overline{v'^2_\theta} + \overline{v'^2_z})$
L_z computational length in the z direction
L_θ computational length in the θ direction
N rotation rate $= V_{\theta\mathrm{w}}/V_\mathrm{m}$
N_r, N_θ, N_z grid points in the r, θ, z directions, respectively
P_j probability of each quadrant (j = 1–4)
p pressure
q_r, q_θ, q_z $q_r = r \cdot v_r$, $q_\theta = r \cdot v_\theta$, $q_z = v_z$
Q_τ friction velocity $= \left(\sqrt{\tau_z^2 + \tau_\theta^2}/\rho\right)^{1/2}$
r, θ, z spatial coordinates in the r, θ, z directions, respectively
R^* radius ratio $= R_1/R_2$
R_1, R_2 radius of inner and outer cylinder, respectively
Re Reynolds number based on characteristic velocity and length scales
Re_τ Reynolds number $= Q_\tau\delta/\nu$
Re_{D_h} Reynolds number $= V_\mathrm{m}D_\mathrm{h}/\nu$
Ri Richardson number
S symmetric component of the velocity gradient tensor
S_{ij} strain-rate tensor
Ta Taylor number
$V_\mathrm{c}, V_\mathrm{m}$ laminar maximum velocity and bulk mean velocity
v_r, v_θ, v_z velocity components in the r, θ, z directions, respectively
V_r, V_θ, V_z mean velocity components in the r, θ, z directions, respectively
y distance from the inner or outer wall

Greeks

δ half width between inner wall and outer wall
δ_{ij} Kronecker delta tensor
Δr minimum grid spacing in the radial direction
Δr_max maximum grid spacing in the radial direction
$\Delta\theta, \Delta z$ grid spacing in the azimuthal and axial directions, respectively
$\overline{\Delta}$ filter width
γ_g mean flow strain rate angle $= \tan^{-1}[(\partial V_\theta/\partial r)/(\partial V_z/\partial r)]$
γ_τ Reynolds shear stress angle $= \tan^{-1}[(\overline{v'_r v'_\theta})/(\overline{v'_r v'_z})]$
λ_2 second largest eigenvalue of $S^2 + \Omega^2$
ν kinematic viscosity
ν_T turbulent eddy viscosity
ν_z streamwise component of eddy viscosity $= -\overline{v'_r v'_z}/(\partial V_z/\partial r)$
ν_θ azimuthal component of eddy viscosity $= -\overline{v'_r v'_\theta}/(\partial V_\theta/\partial r)$
Ω anti-symmetric component of the velocity gradient tensor
ρ density of fluid
τ_z statistically averaged wall shear stress in the streamwise direction at the inner or outer wall
τ_θ statistically averaged wall shear stress in the azimuthal direction at the inner or outer wall
$\hat{\tau}_{ij}$ total stress $= 2(1/Re + \nu_\mathrm{T})\overline{S}_{ij}$
II_b second invariant of $b_{ij} = -(1/2)b_{ij}b_{ji}$
III_b third invariant of $b_{ij} = (1/3)b_{ij}b_{jk}b_{ki}$

Abbreviations

AIM anisotropy invariant map
CFL Courant–Friedrichs–Lewy
DNS direct numerical simulation
LDV laser Doppler velocimetry
LES large-eddy simulation
p.d.f.s probability density functions
Q1, Q2, Q3, Q4 first, second, third and fourth quadrant, respectively
RANS Reynolds-averaged Navier–Stokes
r.m.s. root mean square
SGS subgrid-scale
SP splatting parameter $= (1/r)(\partial v'_\theta/\partial\theta) + \partial v'_z/\partial z$
TBL turbulent boundary layer

Superscripts and Subscripts

$()'$ fluctuating component
$()^+$ normalized by Q_τ, ν
$\overline{()}$ statistically averaged in time and space or filtered value
$()_\mathrm{w}$ values of walls
$()_1$ values of inner wall
$()_\mathrm{rms}$ root mean square value

using the mixing-length model. They showed that the flow development length decreases significantly with increasing rotation rate ($N = V_{\theta w}/V_m$), and confirmed that the mean angular momentum in the center region is almost constant. Torii and Yang (1994) employed several k–ϵ models to study flows through concentric annuli with rotating inner walls. They found that increasing the Taylor number (Ta) amplified the turbulent kinetic energy, resulting in a substantial enhancement of heat transfer. Using a Reynolds stress turbulence model, Rothe and Pfitzer (1997) found a clear enhancement of momentum and heat transfer with increasing rotation rate of the inner tube.

Despite the substantial literature on flows through rotating concentric annuli, little is known about the near-wall turbulent structures in these systems. Furthermore, most numerical studies have used turbulence models which provide rather limited information. The development of computational methods, including direct numerical simulation (DNS) and large-eddy simulation (LES), has led to an increase in numerical studies of turbulent rotating flows. Turbulent rotating flow in concentric annuli can be considered as a three-dimensional TBL. Several DNS and LES investigations of three-dimensional TBL have been carried out. Moin et al. (1990) conducted a DNS of a turbulent channel flow subject to a spanwise pressure gradient. They found that imposition of a spanwise pressure gradient substantially reduced the turbulent kinetic energy, which they attributed to a decrease in the production of turbulent kinetic energy due to suppression of the pressure strain mechanism for inter-component energy transfer. In addition, they found that the introduction of a spanwise pressure gradient gave rise to a decrease in the structure parameter and the lag between the Reynolds shear stress angle and the mean velocity gradient angle. Later, Sendstad and Moin (1992) used the database of Moin et al. (1990) to study the response of the turbulent eddies in a channel flow to the three-dimensionality. Coleman et al. (1996) used the DNS method to simulate shear-driven channel flow. Their results were consistent with the numerical findings described above. Moreover, they claimed that the most significant effect of three-dimensionality is a modification of the near-wall streaks and the interaction between those streaks and quasi-streamwise vortices, rather than a direct modification of the vortices. In other work in this area, Orlandi and Fatica (1997) used DNS to study turbulent flow in a pipe rotating about its axis. In agreement with experimental results, they found that rotation of the pipe reduced the drag. Kannepalli and Piomelli (2000) carried out a LES study of a spatially developing shear-driven TBL. They observed disruption of the outer-layer vortical structures in addition to behavior similar to previous findings.

In the present study, a turbulent rotating flow in a concentric annulus was simulated using LES to elucidate the effect of rotation of the inner wall on the near-wall structure. Particular attention was devoted to the destabilizing effect of the rotational motion on the near-wall turbulent structure. A schematic diagram of the flow configuration is shown in Fig. 1. Three rotation rates ($N = 0.2145$, 0.429 and 0.858) were used and the radius ratio (R^*) was 0.5 for all N. The Reynolds number based on the bulk velocity (V_m) and the hydraulic diameter (D_h) was 8900. Many turbulent statistics were obtained to analyze the near-wall turbulent structures, which were compared with the experimental data of Nouri and Whitelaw (1994). The anisotropy invariant map (AIM) for the Reynolds stress tensor and the invariant function were also analyzed to estimate the anisotropy of the turbulent structure. The non-equilibrium effect of the inner wall rotation was investigated by examining the eddy viscosity ratio and the difference between two characteristic angles. Finally, probability density functions (p.d.f.s) of the velocity fluctuations and splat/anti-splat process were used to shed further light on the effects of inner-wall rotation on the flow fields in concentric annuli.

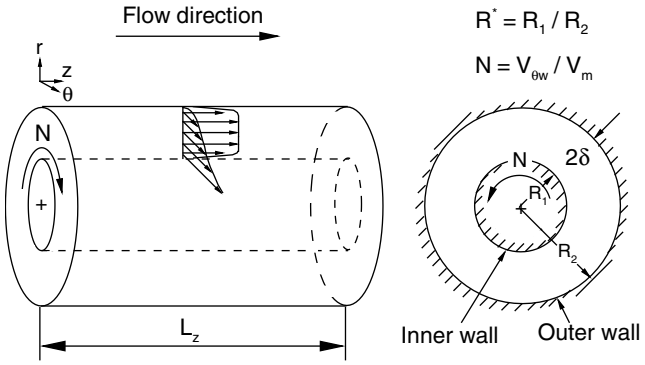

Fig. 1. Schematic diagram and coordinate system.

2. Basic equations and numerical procedures

In the LES formalism, flow variables are decomposed into a large-scale component and a subgrid-scale (SGS) component via a filtering operation. A filtered variable is defined as:

$$\bar{f}(x) = \int_D f(x')G(x,x')\mathrm{d}x', \tag{1}$$

where $G(x)$ is the filter function and D is the computational domain. By applying the filtering operation to the incompressible Navier–Stokes equations and the continuity equation in cylindrical coordinates, one obtains,

$$\frac{1}{r}\frac{\partial \bar{q}_r}{\partial r} + \frac{1}{r^2}\frac{\partial \bar{q}_\theta}{\partial \theta} + \frac{\partial \bar{q}_z}{\partial z} = 0, \tag{2}$$

$$
\begin{aligned}
&\frac{\partial \bar{q}_r}{\partial t}+\frac{\partial}{\partial r}\left(\frac{\bar{q}_r{}^2}{r}\right)+\frac{1}{r^2}\frac{\partial \bar{q}_\theta \bar{q}_r}{\partial \theta}+\frac{\partial \bar{q}_z \bar{q}_r}{\partial z}-\frac{\bar{q}_\theta{}^2}{r^2}\\
&\quad=-r\frac{\partial \bar{p}}{\partial r}+\frac{\partial r\hat{\tau}_{rr}}{\partial r}+\frac{\partial \hat{\tau}_{r\theta}}{\partial \theta}+r\frac{\partial \hat{\tau}_{rz}}{\partial z}-\hat{\tau}_{\theta\theta},\\
&\frac{\partial \bar{q}_\theta}{\partial t}+\frac{\partial}{\partial r}\left(\frac{\bar{q}_r \bar{q}_\theta}{r}\right)+\frac{1}{r^2}\frac{\partial \bar{q}_\theta{}^2}{\partial \theta}+\frac{\partial \bar{q}_z \bar{q}_\theta}{\partial z}+\frac{\bar{q}_r \bar{q}_\theta}{r^2}\\
&\quad=-\frac{\partial \bar{p}}{\partial \theta}+\frac{1}{r}\frac{\partial r^2\hat{\tau}_{r\theta}}{\partial r}+\frac{\partial \hat{\tau}_{\theta\theta}}{\partial \theta}+r\frac{\partial \hat{\tau}_{\theta z}}{\partial z},\\
&\frac{\partial \bar{q}_z}{\partial t}+\frac{1}{r}\frac{\partial \bar{q}_r \bar{q}_z}{\partial r}+\frac{1}{r^2}\frac{\partial \bar{q}_\theta \bar{q}_z}{\partial \theta}+\frac{\partial \bar{q}_z{}^2}{\partial z}\\
&\quad=-\frac{\partial \bar{p}}{\partial z}+\frac{1}{r}\frac{\partial r\hat{\tau}_{rz}}{\partial r}+\frac{1}{r}\frac{\partial \hat{\tau}_{\theta z}}{\partial \theta}+\frac{\partial \hat{\tau}_{zz}}{\partial z},
\end{aligned}
\tag{3}
$$

where $q_r = r \cdot v_r$, $q_\theta = r \cdot v_\theta$, and $q_z = v_z$, and the total stresses are $\hat{\tau}_{ij} = 2(1/Re + v_T)\overline{S}_{ij}$. Here, v_r, v_θ and v_z denote the radial, azimuthal, and axial velocity components, respectively. All the variables are non-dimensionalized by a characteristic length (δ) and velocity scale (V_m), and Re is the Reynolds number. The strain-rate tensor S_{ij} is expressed in terms of the variables q_i as follows:

$$
\begin{pmatrix} S_{rr} & S_{r\theta} & S_{rz} \\ S_{r\theta} & S_{\theta\theta} & S_{\theta z} \\ S_{rz} & S_{\theta z} & S_{zz} \end{pmatrix}
= \begin{pmatrix} \frac{\partial (q_r/r)}{\partial r} & \frac{1}{2}\left[r\frac{\partial (q_\theta/r^2)}{\partial r}+\frac{1}{r^2}\frac{\partial q_r}{\partial \theta}\right] & \frac{1}{2}\left[\frac{1}{r}\frac{\partial q_r}{\partial z}+\frac{\partial q_z}{\partial r}\right] \\ S_{r\theta} & \left[\frac{1}{r^2}\frac{\partial q_\theta}{\partial \theta}+\frac{q_r}{r^2}\right] & \frac{1}{2r}\left[\frac{\partial q_z}{\partial \theta}+\frac{\partial q_\theta}{\partial z}\right] \\ S_{rz} & S_{\theta z} & \frac{\partial q_z}{\partial z} \end{pmatrix}. \tag{4}
$$

Using the eddy viscosity assumption, the turbulent viscosity v_T is expressed as $v_T = C\overline{\Delta}^2 |\overline{S}|$, where $|\overline{S}| = \sqrt{2\overline{S}_{ij}\overline{S}_{ij}}$. In this study, the model coefficient C is determined using the dynamic eddy viscosity model proposed by Germano et al. (1991), as modified and extended by Lilly (1992). In this model, the constant C is not given apriori, but is computed from the flow variables during the simulation. A detailed description of the method for determining the model coefficient can be found in the papers of Germano et al. (1991) and Lilly (1992). The test filter is a box filter in real space, applied by a three-point averaging using Simpson's rule. The total viscosity $1/Re + v_T$ is constrained to be non-negative to ensure numerical stability of the time integration.

The governing Eqs. (2) and (3) are integrated in time using the fractional step method with the implicit velocity decoupling procedure proposed by Kim et al. (2002). Under this approach, the terms are first discretized in time using the Crank-Nicolson method, and then the coupled velocity components in the convection terms are decoupled using the implicit velocity decoupling procedure. The decoupled velocity components are then solved without iteration. Because the implicit decoupling procedure relieves the CFL restriction, the computational time is reduced significantly. The overall accuracy in time is second-order. All the terms are resolved using a second-order central difference scheme in space with a staggered mesh. Details regarding the numerical algorithm can be found in the paper of Kim et al. (2002).

Table 1
Grid resolutions

N	0.2145	0.429	0.858
L_z^+	2937.78	3226.32	3813.30
$L_{\theta_i}^+$	512.73	563.10	1331.09
$L_{\theta_o}^+$	887.12	917.97	2022.05
Δz^+	22.95	16.80	9.93
$(R_1\Delta\theta)^+$	8.01	8.80	10.40
$(R_2\Delta\theta)^+$	13.86	14.34	15.80
Δr_i^+	0.27	0.30	0.35
Δr_o^+	0.23	0.24	0.26
Δr_{max}^+	13.86	15.23	17.99
(N_r, N_θ, N_z)	(65, 64, 128)	(65, 64, 192)	(65, 128, 384)

Periodic boundary conditions are applied in the axial and circumferential directions for the velocity components, and a no-slip boundary condition is imposed at the solid wall. For the $N = 0.2145$ and 0.429 systems, the computational domain was taken as one-quarter of the full cross-section of the concentric annular pipe. However, for the $N = 0.858$ system, the computation was conducted in half of the full cross-section due to the strong inclination of the flow structures induced by the rotation of the inner wall. In all cases the computational length in the streamwise direction was $L_z = 18\delta$. The adequacy of the above computational domains was confirmed by calculating two-point correlations of the fluctuating streamwise velocities in the streamwise (z) and azimuthal (θ) directions for all N. As the value of N was increased, finer grids were required in the axial direction to resolve the re-oriented flow structures; details of the grid resolutions used in the simulations are listed in Table 1. The time step used was $0.03\delta/V_c$ and the total averaging time was $1200\delta/V_c$ in all cases, where V_c is the laminar maximum velocity of the non-rotating flow. This averaging time was sufficient to obtain good statistics. In the wall-normal direction, grid points were clustered according to a hyperbolic tangent distribution.

3. Results and discussion

3.1. Mean flow properties and second-order statistics

Before proceeding further, it is important to first establish the reliability and accuracy of the present numerical simulations. Table 2 lists the mean flow

Table 2
Mean flow parameters

N	0.2145	0.429	0.858
Ta	954.53	1909.05	3818.10
Re_τ (Inner)	163.21	179.24	211.85
Re_τ (Outer)	141.19	146.10	160.91
C_f	0.008913	0.009861	0.012048

parameters for the three N values considered here. Note that the Taylor number (Ta) is defined as $Ta = [(R_2 - R_1)/R_1]^{0.5} V_{\theta w}(R_2 - R_1)/\nu$. In Table 2, the skin friction coefficient based on the average friction velocity ($C_f = \tau_z/\frac{1}{2}\rho V_m^2$) for $N = 0.2145$ is larger than that calculated by Chung et al. (2002) for the non-rotating case. Moreover, this tendency becomes more pronounced as N increases. This is consistent with the results of previous experimental and numerical studies.

Comparison of the mean streamwise velocity distributions calculated in the present study with the experimental data of Nouri and Whitelaw (1994) for $N = 0.429$ (Fig. 2(a)) shows that, except for slight deviations in the center region and near the outer wall, the numerical and experimental results are in satisfactory agreement. It is interesting to note that integration of the experimentally determined profiles in the radial direction does not yield a value of unity. This stands in contrast to the numerical profiles, which yield values of 1.0 upon integration. After rescaling of the experimental data by a normalization process to give an integral in the radial direction of unity, the numerical prediction was in good agreement with the experimental data. Note that, as pointed out by Nouri and Whitelaw (1994), the profiles become flatter and less skewed with increasing N. To further compare our numerical results with experimental findings, Fig. 2(b) depicts the calculated mean azimuthal velocities normalized by the rotational speed of the inner wall along with the corresponding experimental data of Nouri and Whitelaw (1994). The numerical and experimental results show good qualitative agreement; the slight difference between the data sets can be attributed to the coarse resolution used in the LES. Note that the profiles for $N = 0.429$ and 0.858 are inversely proportional to r in the region of $y_1/\delta \approx 0.7$–1.8. This verifies that the mean angular momentum is almost constant in the center region, consistent with the findings of Sharma et al. (1976). In contrast, the velocity gradient undergoes very abrupt changes near the walls.

The logarithmic velocity profiles in the axial direction calculated by LES, along with the profiles calculated by Chung et al. (2002) for the non-rotating case, are shown in Fig. 3. Near the inner wall (Fig. 3(a)), the profiles for the rotating and non-rotating systems differ considerably in the buffer and logarithmic regions. This

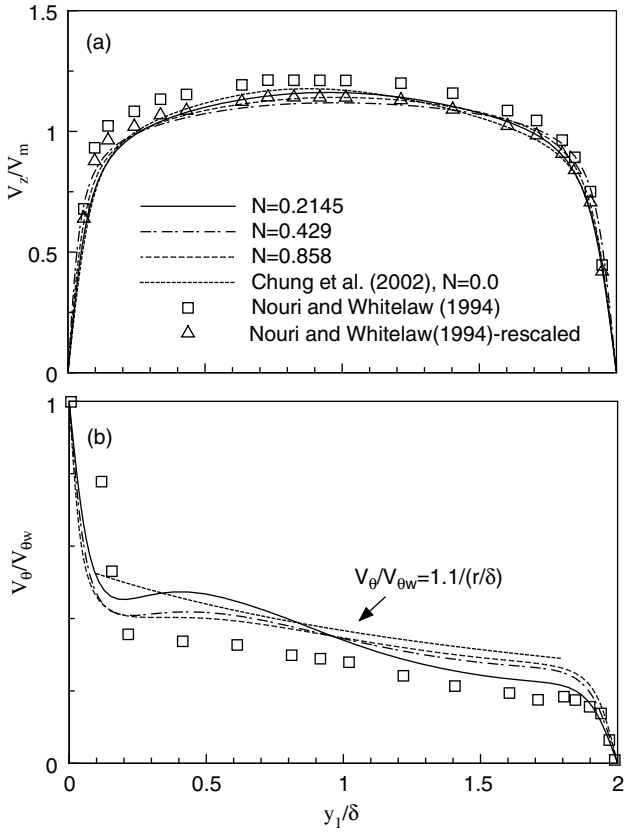

Fig. 2. Distributions of mean streamwise velocity and azimuthal velocity.

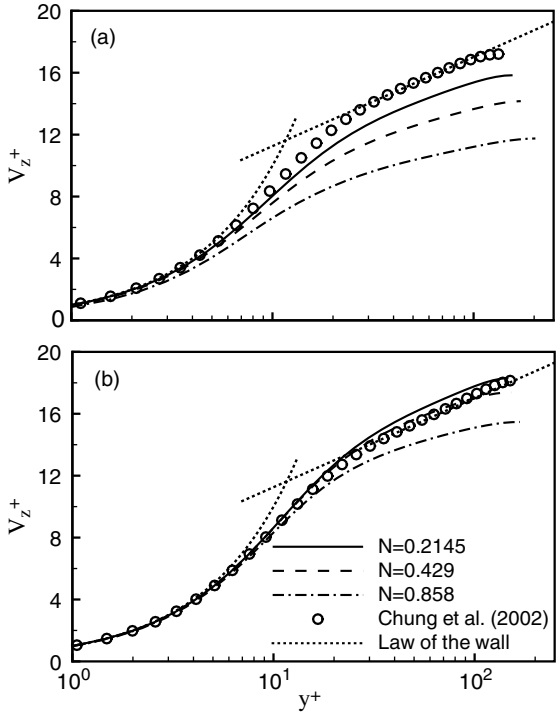

Fig. 3. Mean velocity distributions for the law of the wall: (a) near the inner wall, (b) near the outer wall.

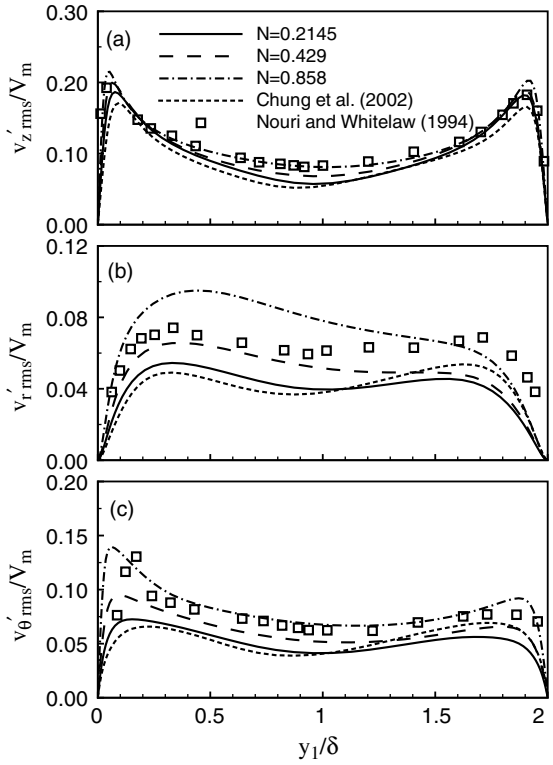

Fig. 4. Root-mean-square velocity fluctuations.

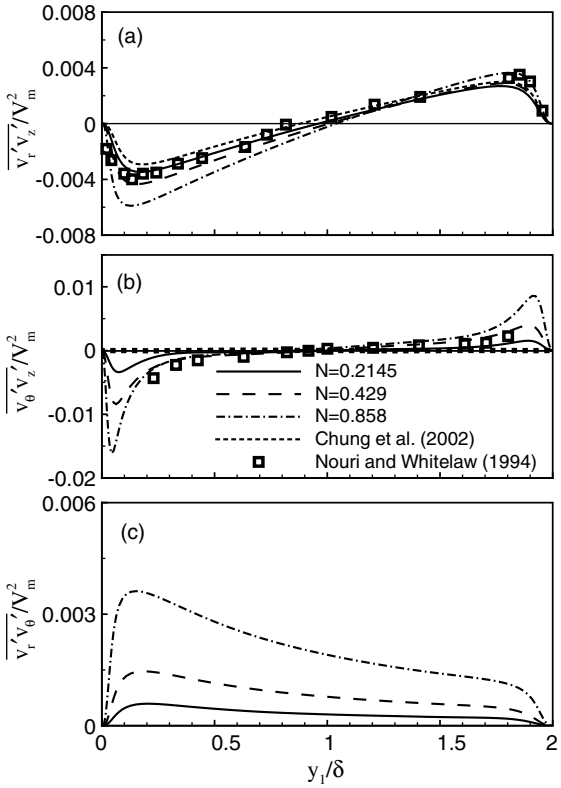

Fig. 5. Distributions of Reynolds shear stresses.

discrepancy becomes more distinct with increasing N. Near the outer wall (Fig. 3(b)), however, these deviations are relatively small. The difference in behavior observed near the inner and outer walls is attributed to the effect of the rotation of the inner wall, which results in an increase in the frictional velocity.

Fig. 4 shows the root-mean-square (r.m.s.) velocity fluctuations normalized by the bulk velocity obtained from our calculations, along with the data of Nouri and Whitelaw (1994) and Chung et al. (2002) for comparison purposes. The calculated fluctuations in the wall-normal (Fig. 4(b)) and azimuthal (Fig. 4(c)) directions show good qualitative agreement with the experimental data. It is clear from Fig. 4 that the velocity fluctuations increase with increasing N. Furthermore, the fluctuation levels are asymmetric, which can be attributed to the destabilizing effect of the centrifugal forces. The Reynolds shear stresses in the global coordinates are displayed in Fig. 5. Unlike the velocity fluctuations, the experimental and numerical Reynolds shear stress results are in good agreement. Similar to the behavior of the r.m.s. velocity fluctuations in Fig. 4, the Reynolds shear stresses increase in strength and become skewed toward the inner wall as N is increased.

When swirl is induced by an inner cylinder rotation in a concentric annulus, the centrifugal force (V_θ^2/r) is reduced with increasing r and the flow becomes unstable. The influence of rotation on turbulent flow may be interpreted as a body force which can stabilize or destabilize turbulence. By using the analogy with stratified flows (Veronis, 1970), one may characterize a rotating turbulent flow in a cylindrical geometry by the Richardson number Ri (Reich and Beer, 1989):

$$Ri = 2\frac{V_\theta}{r^2}\frac{\partial}{\partial r}(rV_\theta)\Big/\left\{\left[\frac{\partial V_z}{\partial r}\right]^2 + \left[r\frac{\partial}{\partial r}\left(\frac{V_\theta}{r}\right)\right]^2\right\}, \qquad (5)$$

where V_θ and V_z denote the mean velocities in the circumferential and axial directions. Fig. 6 shows the distribution of the Richardson number for each N. Ri is negative except in the region of $0.2 \leqslant y_1/\delta \leqslant 0.55$ for $N = 0.2145$. The positive region is increased with increasing N. The sign of Ri is directly related to that of $\partial(rV_\theta)/\partial r$ due the positive V_θ along the whole layer. The swirl effect on turbulent flow is determined by $\partial(rV_\theta)/\partial r$ and $\overline{v'_r v'_\theta}$. In the present study, $\overline{v'_r v'_\theta}$ is positive along the whole layer as shown in Fig. 5(c). Therefore, classification can be made into the two cases according to the signs of $\partial(rV_\theta)/\partial r$ and $\overline{v'_r v'_\theta}$:

Case 1: $\partial(rV_\theta)/\partial r < 0$ and $\overline{v'_r v'_\theta} > 0$,
Case 2: $\partial(rV_\theta)/\partial r > 0$ and $\overline{v'_r v'_\theta} > 0$.

In 'Case 1', $\overline{v'^2_r}$ is increased due to its positive production term $4\overline{v'_r v'_\theta}V_\theta/r$. This promotes the generation term of $\overline{v'_r v'_z}$ $(= -\overline{v'^2_r}\partial V_z/\partial r)$. $\overline{v'_\theta v'_z}$ is generated by the two

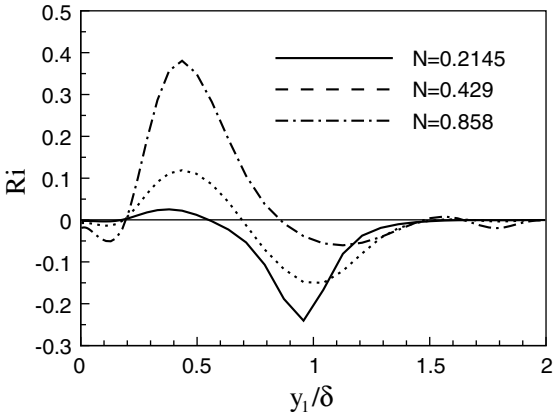

Fig. 6. Profiles of the Richardson numbers.

production terms $-\overline{v_r'v_\theta'}\partial V_z/\partial r$ and $-(\overline{v_r'v_z'}/r)\partial(rV_\theta)/\partial r$. Because these two terms have the same sign as $-\partial V_z/\partial r$, $\overline{v_\theta'v_z'}$ is promoted. $\overline{v_r'v_z'}$ is also enhanced by the increase of $2\overline{v_\theta'v_z'}V_\theta/r$. In 'Case 2', swirl has the effect of promoting $\overline{v_r'v_z'}$ through the generation term $-\overline{v_r'^2}\partial V_z/\partial r$ like 'Case 1', whereas the other generation term $(2\overline{v_\theta'v_z'}V_\theta/r)$ can exert either effect. In the present study, the magnitude of $-\overline{v_r'v_\theta'}\partial V_z/\partial r$ is larger than that of $-(\overline{v_r'v_z'}/r)\partial(rV_\theta)/\partial r$, so $\overline{v_\theta'v_z'}$ is promoted. Thus, the generation term of $\overline{v_r'v_z'}$ $(=2\overline{v_\theta'v_z'}V_\theta/r)$ is also enhanced. It should be mentioned that the swirl by an inner cylinder rotation has the effect of promoting momentum transport. Details regarding the swirl effect on turbulent flow can be found in Hirai and Takagi (1995). The effect of the azimuthal movement of the wall, which takes place in the three-dimensional TBL or channel flow, is different from that of the inner wall rotation in a concentric annulus due to the different transverse curvature.

3.2. Turbulence anisotropy and non-equilibrium effect

To assess the effects of rotating the inner wall on the turbulence structure, we analyzed the near-wall turbulence anisotropy. The interest in turbulence anisotropy is motivated not only by the better understanding of the turbulence structure but also by the development of nonlinear turbulence models. A convenient way to characterize flow anisotropy is through the Reynolds stress anisotropy tensor (Lumley and Newman, 1977):

$$b_{ij} = \overline{u_i'u_j'}/2k - \delta_{ij}/3, \tag{6}$$

where $k \equiv 0.5\overline{u_i'u_i'}$ is the average turbulent kinetic energy and δ_{ij} is the Kronecker delta tensor. For isotropic turbulence, all elements of b_{ij} vanish. The diagonal elements of b_{ij} are restricted to $-1/3 < b_{ij} < 2/3$. The second and third invariants of b_{ij} are given by

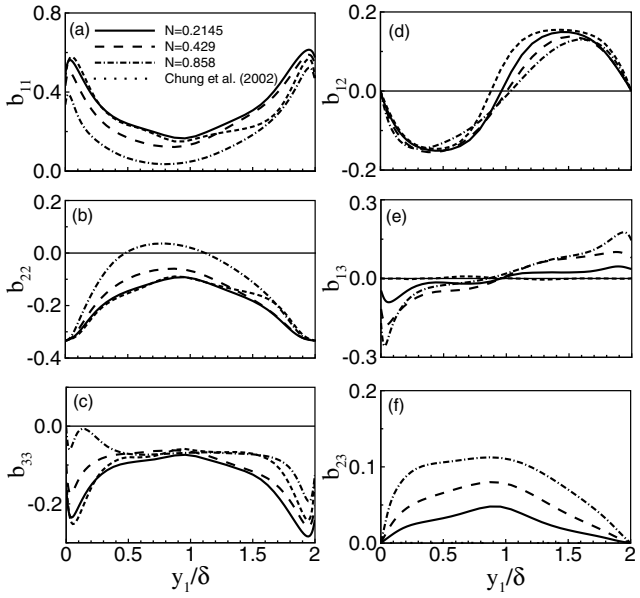

Fig. 7. Reynolds stress anisotropy tensor b_{ij}.

$$\mathrm{II}_b = -\frac{1}{2}b_{ij}b_{ji}, \tag{7}$$

$$\mathrm{III}_b = \frac{1}{3}b_{ij}b_{jk}b_{ki}. \tag{8}$$

The six components of the Reynolds stress anisotropy tensor b_{ij} are plotted in Fig. 7. The salient feature of these plots is that the diagonal terms of b_{ij} shift closer to the isotropic state ($b_{ij} = 0$) as N increases. Note that, at $N = 0.858$, b_{33} (Fig. 7(c)) exhibits a double peak near the inner wall because, in this region, the increase of the azimuthal velocity fluctuation is larger than that of the turbulent kinetic energy. On the other hand, enhanced anisotropy is found in the off-diagonal terms of b_{ij}, except for b_{12} in the center region. The isotropy in the diagonal terms is attributed to the augmentation of the intercomponent energy transfer by the rotation of the inner wall.

Lumley and Newman (1977) have shown that the cross plots of the invariants $-\mathrm{II}_b$ and III_b for axisymmetric turbulence and for two-component turbulence define the AIM that bounds all physically realizable turbulence. In the AIM, turbulence must exist within the area bounded by three lines: an upper straight line ($G = 1/9 + \mathrm{II}_b + 3\mathrm{III}_b = 0$) representing the state of two-component turbulence, and left and right boundaries ($A_b = -(\mathrm{III}_b/2)/(\mathrm{II}_b/3)^{3/2} = \pm 1$) originating from the bottom cusp ($-\mathrm{II}_b = \mathrm{III}_b = 0$), which correspond to two types of axisymmetric turbulence. The left and right boundaries correspond to 'disk-like' and 'rod-like' turbulence states, respectively (Antonia et al., 1991), and the bottom cusp characterizes three-component isotropic turbulence.

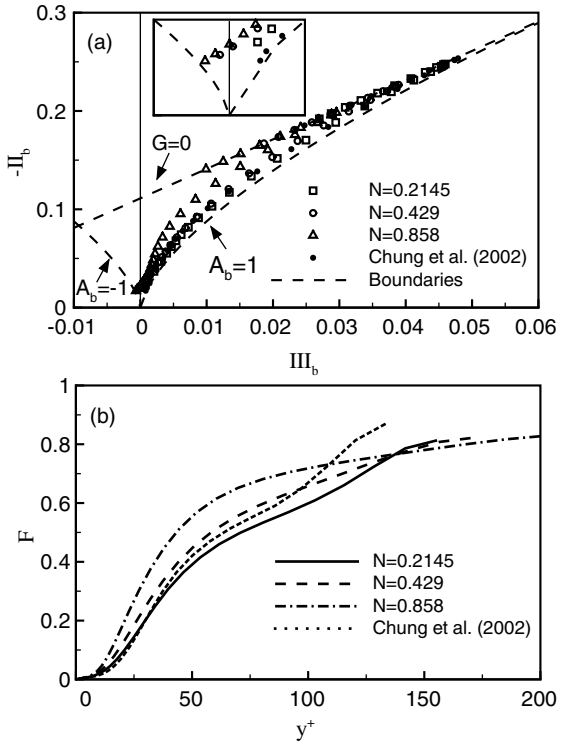

Fig. 8. Anisotropy invariant map for the Reynolds stress tensor and anisotropy invariant function $F = 1 + 9\mathrm{II}_b + 27\mathrm{III}_b$.

Fig. 8(a) shows the AIM for the Reynolds stress tensor, including data for the non-rotating case (Chung et al., 2002) for comparison. The calculated data show all of the characteristics of near-wall turbulence anisotropy. For $N = 0.0$, the turbulence varies from a two-component turbulence state near the wall to an almost isotropic state in the center region. As N increases, the flow becomes more isotropic in the center region. It is notable that, for $N = 0.858$, the turbulence structure approaches a 'disk-like' state near the center region. This is due to the smaller value of v'_θ in comparison to the other velocity components. To assess the changes in the AIM with varying N, we monitored the maximum values of $-\mathrm{II}_b$ and III_b at several N; these values are summarized in Table 3. Compared with the $N = 0.0$ system, the maximum values of $-\mathrm{II}_b$ and III_b for $N = 0.858$ are 22% and 38% lower, respectively. Another estimate of the overall anisotropy in the Reynolds stress tensor is given by the function $F = 1 + 9\mathrm{II}_b + 27\mathrm{III}_b$, which is a measure of the approach to either two-dimensional turbulence ($F = 0$) or three-component turbulence ($F = 1$). It is clear from

Table 3
Maximum values of $-\mathrm{II}_b$ and III_b

N	0.2145	0.429	0.858	0.0
$-\mathrm{II}_b$	0.24777	0.22659	0.19842	0.25361
III_b	0.04597	0.03892	0.02956	0.04789

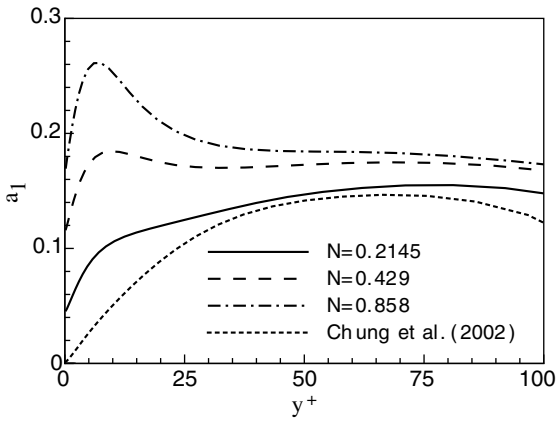

Fig. 9. Structure parameter a_1.

Fig. 8(b) that, across the layer, F shifts closer to 1 with increasing N.

To evaluate the efficiency of the eddies in producing turbulent shear stresses for a given amount of turbulence energy, we consider the structure parameter $a_1 = (\overline{v'_r v'_z}^2 + \overline{v'_r v'_\theta}^2 + \overline{v'_\theta v'_z}^2)^{1/2}/2k$, as shown in Fig. 9. In the near-wall region, a_1 increases sharply as N is increased. This trend near the wall appears to be due to the increase of the Reynolds shear stresses with increasing N, rather than to a diminishing of the turbulent kinetic energy. Similar behavior is still discernible away from the wall. However, this behavior is the opposite of that found in numerical simulations of rotating pipes and three-dimensional TBLs over a flat plate (Orlandi and Fatica, 1997; Kannepalli and Piomelli, 2000), suggesting that the instability associated with the rotation of the inner wall in a concentric annulus enables more efficient extraction of shear stress from a given amount of turbulent kinetic energy. These changes in the second-order statistics give detailed information that can be used to improve turbulence models related to swirling flows.

To determine whether the turbulence is in equilibrium with the mean flow, we examined the eddy viscosity ratio and the difference between the mean flow strain rate angle and the Reynolds shear stress angle (Fig. 10(a) and (b), respectively). The streamwise and azimuthal components of the eddy viscosity are defined as:

$$\nu_z = -\frac{\overline{v'_r v'_z}}{\partial V_z/\partial r}, \quad \nu_\theta = -\frac{\overline{v'_r v'_\theta}}{\partial V_\theta/\partial r}. \tag{9}$$

The mean flow strain rate angle and the Reynolds shear stress angle are defined as:

$$\gamma_g = \tan^{-1}\frac{\partial V_\theta/\partial r}{\partial V_z/\partial r}, \quad \gamma_\tau = \tan^{-1}\frac{\overline{v'_r v'_\theta}}{\overline{v'_r v'_z}}. \tag{10}$$

Discontinuities in the mean flow strain rate angle (Fig. 10(a)) indicate that the eddy viscosity is strongly anisotropic in the non-equilibrium regions. This phenomenon

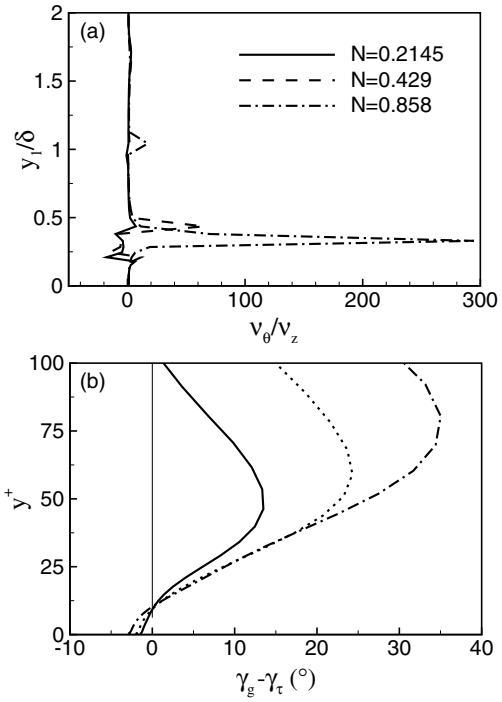

Fig. 10. Profiles of eddy viscosity ratios and flow angles.

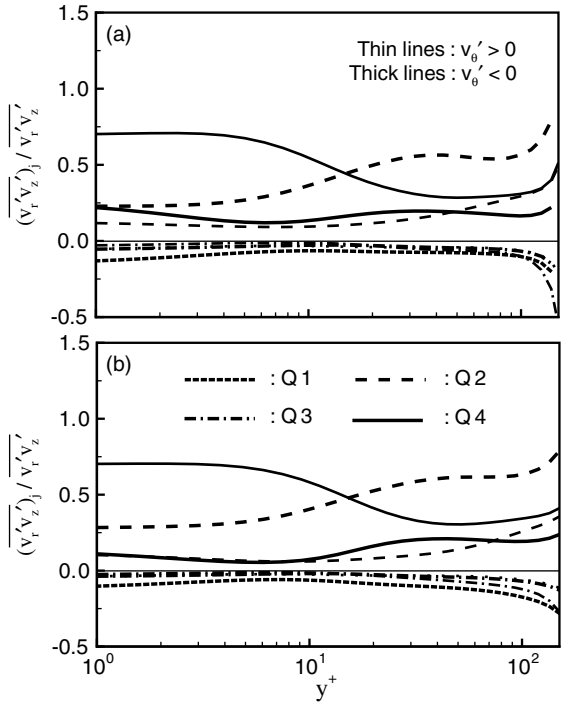

Fig. 11. Reynolds shear stress for each octant normalized by the mean Reynolds shear stress: (a) $N = 0.429$, (b) $N = 0.858$.

is mainly due to the fact that the spanwise shear $\partial V_\theta/\partial r$ goes to zero. It demonstrates that the simple eddy-viscosity-type turbulence models for the RANS (Reynolds-averaged Navier–Stokes) equations are ill suited to predicting flows of this type. Furthermore, as can be seen in Fig. 10(b), the shear stress angle lags behind the strain angle, as was observed in previous studies of three-dimensional TBLs (Moin et al., 1990; Kannepalli and Piomelli, 2000). This is a further indication that the turbulence is not in equilibrium with the mean flow gradients.

3.3. Octant analysis and joint p.d.f.s of velocity fluctuations

Octant analysis of the Reynolds shear stress provides detailed information on the contribution of flow events to the production (consumption) of turbulent kinetic energy in three-dimensional turbulent flows (Sendstad and Moin, 1992). In octant analysis, the Reynolds shear stress is divided into eight categories according to the signs of v_r', v_θ' and v_z'. The fractional distribution to the Reynolds shear stress $\overline{v_r'v_z'}$ from each octant is shown in Fig. 11 for two rotation rates. In this figure, thin and thick lines denote positive and negative values of v_θ', respectively. For both rotation rates, the crossover point between the dominance of ejection (Q2) and sweep (Q4) events is located at $y^+ \approx 15$. It should be noted that, near the wall, Q4 events of negative v_θ' predominate over those of positive v_θ', whereas Q2 events of positive v_θ' contribute to the Reynolds shear stress to a greater extent than those of negative v_θ'. This tendency is particularly pronounced at $N = 0.858$, possibly due to the reinforcement of coherent structure near the wall by the rotation of the inner surface. To separate the effect of the number of occurrences from the octant analysis, the probability distributions of the Reynolds shear stress for each octant were determined (Fig. 12). These distributions indicate that Q4 events of negative v_θ' occur more frequently than those of positive v_θ', whereas Q2 events of positive v_θ' occur more frequently than those of negative v_θ'.

To better comprehend the modification of the flow structures by the rotation, we consider the p.d.f.s of the velocity fluctuations. The joint p.d.f. contours of v_z' and v_r' (Fig. 13(a)) show that the rotation increases the events in the second (ejections) and fourth (sweeps) quadrants and that the contribution of events with fluctuations of equal sign decreases. This is consistent with the result of the octant analysis for Reynolds shear stress $\overline{v_r'v_z'}$, and is in accord with the decrease observed in $\overline{v_r'v_z'}$ near the inner wall in Fig. 5(a).

The joint p.d.f.s of v_z' and v_θ', and of v_r' and v_θ', also show rotation-induced changes in the flow structure. In the non-rotating flow, symmetry dictates that the Reynolds stresses $\overline{v_z'v_\theta'}$ and $\overline{v_r'v_\theta'}$ are zero. The behavior of these joint p.d.f.s for $N = 0.0$, depicted as contour plots in Figs. 13(b) and 14(a), correctly represent the

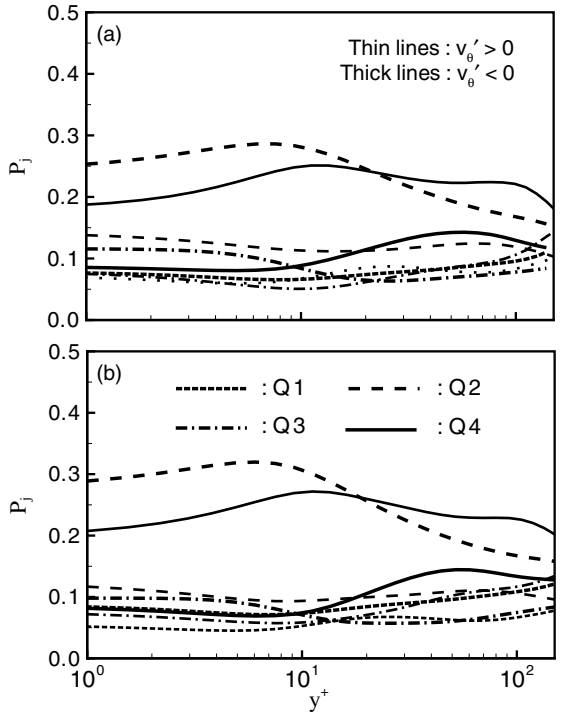

Fig. 12. Probability distribution of Reynolds shear stress for each octant: (a) $N = 0.429$, (b) $N = 0.858$.

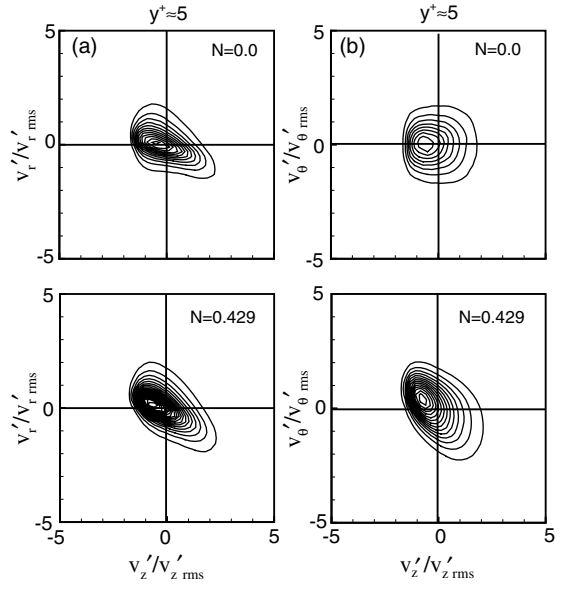

Fig. 13. Joint p.d.f. of (a) v_z' and v_r', (b) v_z' and v_θ'.

cancellations between the contributions. The joint p.d.f. of v_z' and v_θ' for $N = 0.429$ (Fig. 13(b)) shows that the negative $\overline{v_z'v_\theta'}$ seen in Fig. 5(b) is due to an increase of intense negative/positive v_z' correlated with intense v_θ' of the opposite sign (quadrants 2 and 4). In addition, the events in the fourth quadrant make a greater contribution to $\overline{v_z'v_\theta'}$ than those in the second quadrant. These observations indicate that the rotation increases the correlation between high-speed streaks and regions of negative v_θ'. When a fluid particle with high speed moves towards the rotating wall, it mostly has positive v_z' and negative v_θ' due to the relatively low V_z and high V_θ velocities near the wall. Thus, the rotation promotes the correlation between high speed streaks and negative v_θ'. Additionally, the rotation disrupts the symmetry, as is evident in the joint p.d.f. for $N = 0.429$ (Fig. 14(a)). This plot implies that large negative azimuthal fluctuations are associated with the strong in-rush event, and that large positive azimuthal fluctuations occur when there is an ejection. This reflects the result of the positive $\overline{v_r'v_\theta'}$ as shown in Fig. 5(c).

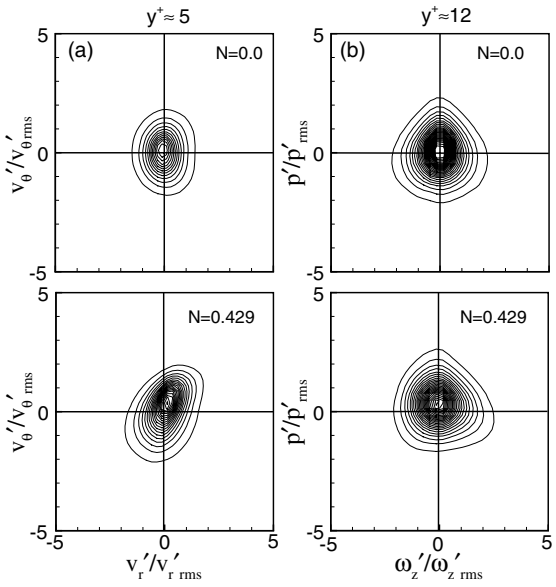

Fig. 14. Joint p.d.f. of (a) v_r' and v_θ', (b) ω_z' and p'.

In a study of a spatially evolving TBL, Robinson (1991) noticed a strong correlation between low-pressure regions and streamwise vortices. In another study of a spatially evolving TBL, Kim (1989) examined the joint p.d.f. between pressure and streamwise vorticity, and found that the peaks of ω_z' are associated with large negative pressure fluctuations but not vice versa. Similar correlations are evident in the joint p.d.f. for $N = 0.0$ (Fig. 14(b)). At $N = 0.429$, large negative pressure fluctuations are more correlated with the large positive vorticity fluctuations than the large negative ones. This asymmetry in the joint p.d.f. between ω_z' and p' may be caused by the rotation of the inner wall.

3.4. Splat/anti-splat process

A key finding of the present study is that the turbulent statistics of the rotating system are greater in magnitude than those of the non-rotating system. Our

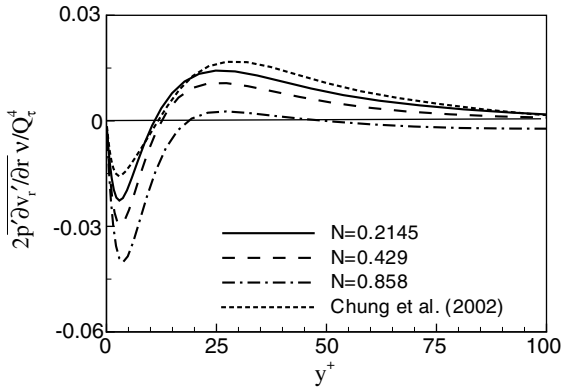

Fig. 15. Pressure strain terms in the budget of $\overline{v_r' v_r'}$.

investigation of the joint p.d.f.s of the velocity fluctuations revealed that this difference is associated with the increase of ejection and sweep motions with increasing N. The splatting mechanism is considered to be closely linked to the sweep events near the wall. Splatting is defined as a net energy transfer from the vertical component (v_r') of the turbulence intensity to the horizontal components (v_θ' and v_z') (Moin and Kim, 1982). The splatting effect, which is correlated with sweep events and vorticity stretching, produces a flow pattern similar to that of a jet impinging upon a wall. In the present study, we carried out a quantitative investigation to explain in detail the alteration of the splatting effect in the flow due to the rotation of the inner wall.

In past studies, the pressure strain terms in the budget of $\overline{v_r' v_r'}$ have been exploited to explain the splatting effect (Moin and Kim, 1982; Chung and Sung, 2003). Fig. 15 shows the pressure strain terms in the budget of $\overline{v_r' v_r'}$. The reversal of the sign of the pressure strain term near the wall is a clear indicator of the splatting effect. It is interesting to note that the pressure strain term near the walls decreases with increasing N. This indicates that rotation of the inner wall strengthens the splatting events.

To explain the difference in the strength of the splatting events in the rotating and non-rotating systems, we calculated the p.d.f.s of the splat/anti-splat process, where a splat event transfers energy from the normal velocity component to the two tangential velocity ones, and an anti-splat event is a counterpart of a splat one. We follow the approach of Chung and Sung (2003), which employs the parameter $((1/r)(\partial v_\theta'/\partial\theta) + \partial v_z'/\partial z)$, hereinafter referred to as SP, from the continuity equation. SP is positive for splat events, but negative for anti-splat events.

The p.d.f.s of the splat/anti-splat process at $y^+ \approx 5$, weighted by the absolute value of SP normalized by its r.m.s. value, are depicted in Fig. 16(a). In this figure, the superscript (*) in the label for the horizontal axis indicates that the quantity is normalized by its r.m.s. value. The weighting of the p.d.f.s enhances the contributions of the strong splatting events. The splat events at $N = 0.429$ in Fig. 16(a) are stronger than those reported by Chung and Sung (2003) for the $N = 0.0$ system, indicating that the sweep events are stronger in the rotating system compared to the non-rotating one.

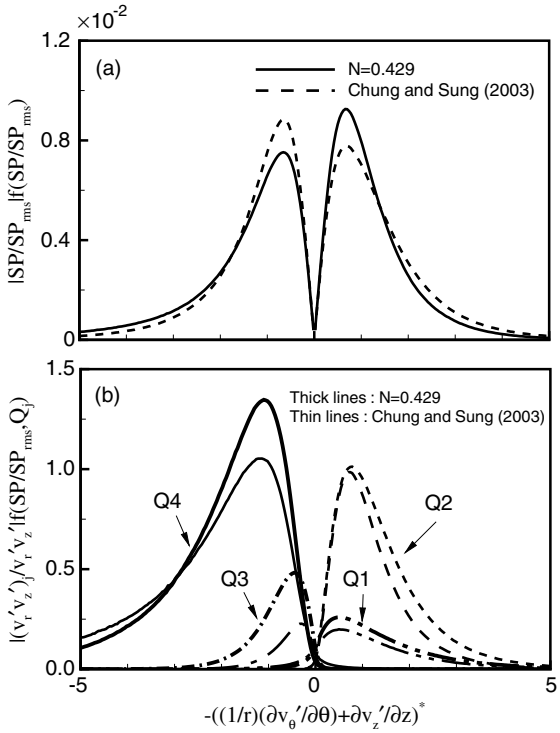

Fig. 16. Weighted p.d.f.s of the splat/anti-splat process and those for each quadrant of Reynolds shear stress.

To better elucidate the close relation between sweep and splat events, the p.d.f.s of the splat/anti-splat process about each quadrant of the Reynolds shear stress were calculated (Fig. 16(b)). Here, Q_j ($j = 1$–4) represents the four quadrants according to the signs of v_r' and v_z' (Chung et al., 2002). In Fig. 16(b), thick and thin lines denote the profiles of the rotating and non-rotating cases, respectively. Note that, consistent with the results of the quadrant analysis of the Reynolds shear stress conducted by Chung et al. (2002), the profiles of Q2 and Q4 are of greater magnitude than those of Q1 and Q3. Inspection of the distributions of Q4 in Fig. 16(b) reveals that the $N = 0.429$ system gives rise to the strongest splat events. Fig. 16 gives a sufficiently complete picture of the strong connection between sweep and splat events.

Finally, we calculated instantaneous iso-surfaces of $-\lambda_2$ by the vortex identification method of Jeong and Hussain (1995), which are shown in Fig. 17. For the $N = 0.429$ system, the quasi-streamwise vortices are tilted in the direction of the wall shear stress and are more activated than those of $N = 0.0$. These iso-surfaces provide further evidence that strong sweep and ejection

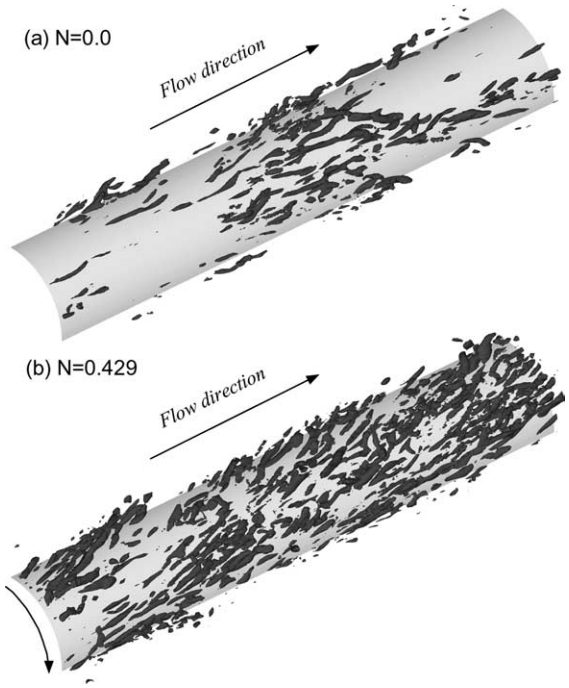

Fig. 17. Iso-surfaces of $-\lambda_2$ by the vortex identification method (a) $N = 0.0$, (b) $N = 0.429$.

motions occur more frequently near the inner wall when it is rotating.

4. Summary and conclusions

In the present study, the LES method was used to simulate turbulent flow in concentric annuli with inner wall rotation at $Re_{D_h} = 8900$ and $R^* = 0.5$ for three rotation rates ($N = 0.2145$, 0.429 and 0.858). The main emphasis of this work was on the destabilization of the near-wall turbulent structures due to rotation of the inner wall. The calculated mean velocity and second-order statistics were in good agreement with previous experimental data (Nouri and Whitelaw, 1994). The simulations showed that, when the inner wall is rotated, the slope of the mean velocity profile near the inner wall is lower in the logarithmic region. The overall turbulent statistics were found to be of greater magnitude for the rotating case than for the non-rotating one, with this tendency becoming more apparent at higher rotation rate. The anisotropy invariant map for the Reynolds stress tensor and the invariant function F indicated that the flow becomes more isotropic in the center region as N increases. Investigation of the structure parameter revealed that the efficiency of the eddies in producing turbulent shear stresses for a given amount of turbulence energy becomes larger at higher N. The stress angle was found lag behind the strain angle, consistent with previous studies on three-dimensional boundary layers. The anisotropy of the eddy viscosity confirmed that the flow was in a non-equilibrium state. Finally, p.d.f.s of velocity fluctuations and the splat/anti-splat process were scrutinized to construct a more complete picture of the effect on the flow fields of rotating the inner wall. The present numerical results show that the alteration of the turbulent structures can be attributed to the destabilizing effect of rotation of the inner wall, which gives rise to an augmentation of sweep and ejection events.

Acknowledgement

This work was supported by a grant from the National Research Laboratory of the Ministry of Science and Technology, Korea.

References

Antonia, R.A., Kim, J., Browne, L.W.B., 1991. Some characteristics small-scale turbulence in a turbulent duct flow. J. Fluid Mech. 233, 369–388.

Chung, S.Y., Sung, H.J., 2003. Direct numerical simulation of turbulent concentric annular pipe flow. Part 2: Heat transfer. Int. J. Heat Fluid Flow 24, 399–411.

Chung, S.Y., Rhee, G.H., Sung, H.J., 2002. Direct numerical simulation of turbulent concentric annular pipe flow. Part 1: Flow field. Int. J. Heat Fluid Flow 23, 426–440.

Coleman, G.N., Kim, J., Le, A.T., 1996. A numerical study of three-dimensional wall-bounded flows. Int. J. Heat Fluid Flow 17, 333–342.

Escudier, M.P., Gouldson, I.W., 1995. Concentric annular flow with centerbody rotation of a Newtonian and a shear-thinning liquid. Int. J. Heat Fluid Flow 16, 156–162.

Germano, M., Piomelli, U., Moin, P., Cabot, W.H., 1991. A dynamic subgrid-scale eddy viscosity model. Phys. Fluids A 3, 1760–1765.

Hirai, S., Takagi, T., 1995. Parameters dominating swirl effects on turbulent transport derived from stress-scalar-flux transport equation. Int. J. Heat Mass Trans. 38, 2175–2182.

Jeong, J., Hussain, F., 1995. On the identification of a vortex. J. Fluid Mech. 285, 69–94.

Kannepalli, C., Piomelli, U., 2000. Large-eddy simulation of a three-dimensional shear-driven turbulent boundary layer. J. Fluid Mech. 423, 175–203.

Kaye, J., Elgar, E.C., 1958. Modes of adiabatic and diabatic fluid flow in an annulus with an inner rotating cylinder. Trans. ASME: J. Heat Transfer 80, 753–765.

Kim, J., 1989. On the structure of pressure fluctuations in simulated turbulent channel flow. J. Fluid Mech. 205, 421–451.

Kim, K., Baek, S.-J., Sung, H.J., 2002. An implicit velocity decoupling procedure for the incompressible Navier–Stokes equations. Int. J. Numer. Meth. Fluids 38, 125–138.

Lilly, D.K., 1992. A proposed modification of the Germano subgrid-scale closure method. Phys. Fluids A 4, 633–635.

Lumley, J.L., Newman, G.R., 1977. The return to isotropy of homogeneous turbulence. J. Fluid Mech. 82, 161–178.

Moin, P., Kim, J., 1982. Numerical investigation of turbulent channel flow. J. Fluid Mech. 118, 341–377.

Moin, P., Shih, T.H., Driver, D., Mansour, N.N., 1990. Direct numerical simulation of a three-dimensional turbulent boundary layer. Phys. Fluids A 2, 1846–1853.

Nouri, J.M., Whitelaw, J.H., 1994. Flow of Newtonian and non-Newtonian fluids in a concentric annulus with rotation of the inner cylinder. Trans. ASME: J. Fluids Eng. 116, 821–827.

Orlandi, P., Fatica, M., 1997. Direct simulations of turbulent flow in a pipe rotating about its axis. J. Fluid Mech. 343, 43–72.

Reich, G., Beer, H., 1989. Fluid flow and heat transfer in an axially rotating pipe—I. Effect of rotation on turbulent pipe flow. Int. J Heat Mass Trans. 32, 551–562.

Robinson, S.K., 1991. Coherent motions in the turbulent boundary layer. Ann. Rev. Fluid Mech. 23, 601–639.

Rothe, T., Pfitzer, H., 1997. The influence of rotation on turbulent flow and heat transfer in an annulus between independently rotating tubes. Heat Mass Trans. 32, 353–364.

Sendstad, O., Moin, P., 1992. The near wall mechanics of three-dimensional turbulent boundary layers. Rep. TF-57, Thermosciences division, Department of Mechanical Engineering, Stanford University.

Sharma, B.I., Launder, B.E., Scott, C.J., 1976. Computation of annular turbulent flow with rotating core tube. Trans. ASME: J. Fluids Eng. 98, 753–758.

Taylor, G.I., 1923. Stability of a viscous fluids contained between two rotating cylinders. Philos. Trans. A 223, 289–343.

Torii, S., Yang, W.J., 1994. Numerical study on turbulent flow and heat transfer in circular Couette flows. Numer. Heat Trans. Part A: Appl. 26, 321–336.

Veronis, G., 1970. The analogy between rotating and stratified fluids. Ann. Rev. Fluid Mech. 2, 37–66.

Yamada, Y., 1962. Resistance of a flow through an annulus with an inner rotating cylinder. Bull. JSME 5, 302–310.